

A periodic representation of the interface for the volume of fluid method

Joris C.G. Verschaeve

*Department of Energy and Process Engineering,
Norwegian University of Science and Technology,
N-7491 Trondheim, Norway
joris.verschaeve@ntnu.no*

Abstract

We extend the volume of fluid method for the computation of two-phase flow to a higher order accurate method in two dimensions. The interface reconstruction by the PLIC method is thereby replaced by a periodic interface reconstruction. The advection step is reformulated and extended to higher order in order to account for the present interface representation. This periodic interface reconstruction describes the interface in terms of higher order periodic B-splines. Numerical tests verify that the theoretical order of convergence is indeed exhibited by the present method.

Key words: B-Splines, Two-phase Flow, VOF, High Order Accuracy

1. Introduction

Two-phase flow can be found in many industrial applications. A popular method for the computation of two-phase flow is the volume of fluid method (VOF) [20, 2].

The volume fraction, the central object of the volume of fluid method, denotes the ratio of the volume (area in 2D) occupied by one phase in a cell of

the computational domain to the cell volume (cell area in 2D). The volume of fluid method can be subdivided into two steps: the interface reconstruction step and the advection step. The interface reconstruction step computes the interface position at time t using the volume fraction field at time t . The advection step advects the volume fraction field from time t to time $t + \Delta t$ using the reconstructed interface at time t . The volume of fluid method has its origins in the works of [7] and [14]. Substantial improvement of the interface reconstruction has been achieved with the piecewise linear interface computation (PLIC) method by Youngs [26] in 1982. However, the resulting interface is approximated by piecewise straight lines which makes it necessary to estimate the curvature by additional approximation schemes, for example the height function method [6, 10, 9, 11]. In order to obtain a more smooth interface, Price *et al.* in 1998 [17] derived a method replacing the straight lines by parabolas. Due to the fact that a numerical minimization has to be performed in each cell to find all the coefficients of the interface parabola, the method enjoys less popularity. More recently, in 2004, Lopez *et al.* [12] used a parametric cubic spline interpolation through the midpoints of the PLIC interface lines and obtained a smoother description of the interface. However, although cubic splines are known to interpolate a function with fourth order accuracy, their method inherits the second order accuracy of the PLIC method for the test cases presented in [12] since it is based on the same approach. A further development of this interface reconstruction using splines to improve the interface obtained by the piecewise lines of the PLIC method has been presented in [8] using quadratic splines. Both approaches are, however, based on the PLIC method for reconstruction and advection and share

therefore also the drawbacks of the PLIC method. Another approach replacing this time the PLIC method has been presented in [23, 22, 24], where the interface is divided into segments and each segment is reconstructed globally. This allowed for a more accurate description of the interface. A drawback of this method is however the need to choose a division of the interface into segments.

In the present discussion we shall modify the approach presented in [23, 22, 24] by deriving a periodic description of the interface separating two immiscible liquids in two dimensions. The present method is, as the method in [23, 22, 24], a global method opposed to the PLIC method which uses only local information. The interface in the present discussion is represented indirectly by two functions depending on a periodic parameter. The actual position or other quantities, such as the normal or the local curvature at the interface, are then derived from these two functions. The advection step is adapted to the present interface representation.

The present discussion is organized as follows: The present interface representation is derived in the next section, section 2. Periodic B-splines are used to approximate the interface, cf. section 3. In section 4, the advection step is presented. The numerical verification is done in section 5. Finally, the present discussion is concluded in section 6.

2. A periodic representation of the interface

In the present discussion we treat the case of a two dimensional drop of blue fluid enclosed in red fluid, cf. figure 1. The red fluid occupies the domain Ω_{red} , whereas the blue fluid occupies the domain Ω_{blue} . These two domains are separated by a common boundary, the interface I . The central

problem of the volume of fluid method is to compute the temporal evolution of the interface I when subjecting the fluids to a velocity field \vec{u} :

$$\vec{u} = \begin{pmatrix} u_x(x, y, t) \\ u_y(x, y, t) \end{pmatrix}. \quad (1)$$

Since we are dealing with incompressible fluids, the velocity is solenoidal. In the present discussion we assume that the interface I can be described by a periodic line l . We exclude topological changes in the present discussion. In addition any third phase should not be present in order to avoid contact points. We also assume the line l to be sufficiently regular. As for polygons, cf. [1], the area of a domain Ω_{blue} , enclosed by a line l , can be computed by means of a function \vec{F} :

$$\vec{F}(\vec{x}) = \frac{1}{2}\vec{x}, \quad (2)$$

where \vec{x} is the position vector of a point. The divergence of (2) is unity, as can be verified straightforwardly. Having now a periodic parametrization of the line l :

$$l : \vec{x}(s) = \begin{pmatrix} x(s) \\ y(s) \end{pmatrix}, \quad s \in [0, 2\pi) \quad (3)$$

the area V of Ω_{blue} can be expressed by:

$$V = \int \int_{\Omega_{blue}} dx dy = \int \int_{\Omega_{blue}} \nabla \cdot \vec{F} dx dy = \int_0^{2\pi} \vec{F} \cdot \vec{n} ds' = \frac{1}{2} \int_0^{2\pi} x(s')y'(s') - x'(s')y(s') ds', \quad (4)$$

where the periodicity of the line has, without loss of generality, been chosen to be 2π . It is, in addition, implied that the tangential on l points in counter clockwise direction. We now define two functions $\alpha(s)$, resp. $\beta(s)$ by:

$$\alpha(s) := \frac{1}{2} \int_{s_0}^s x(s')y'(s') - x'(s')y(s') ds', \quad (5)$$

$$\beta(s) := x(s)y(s). \quad (6)$$

The derivatives of $\alpha(s)$, resp. $\beta(s)$ are then given by:

$$\alpha'(s) = \frac{1}{2}(x(s)y'(s) - x'(s)y(s)) \quad (7)$$

$$\beta'(s) = x'(s)y(s) + x(s)y'(s). \quad (8)$$

Since the position $\vec{x}(s)$ of a point on the interface is periodic in s , we conclude that the derivatives α' , resp. β' are also periodic in s . The position $(x(s), y(s))$ of a point on the interface on the other hand can then be recovered by the following expressions:

$$\frac{x'}{x} = \frac{\frac{1}{2}\beta' - \alpha'}{\beta} =: a(s), \quad (9)$$

$$\frac{y'}{y} = \frac{\frac{1}{2}\beta' + \alpha'}{\beta} =: b(s). \quad (10)$$

Integrating equations (9) and (10) with respect to s gives us then the final result:

$$x(s) = x_0 \exp \int_{s_0}^s a(s') ds', \quad (11)$$

$$y(s) = y_0 \exp \int_{s_0}^s b(s') ds', \quad (12)$$

where (x_0, y_0) is the position of the interface for $s = s_0$. In order for equations (9) and (10) to be well defined we have to choose a coordinate system having the region Ω_{red} in the positive quadrant sufficiently far from the origin. The area V included by the interface is then given by:

$$V = \alpha(2\pi). \quad (13)$$

The strategy of the present method is to represent the interface of the drop by the functions α , resp. β and to obtain the position of the interface by

formulae 11, resp. 12. A normal \vec{n} on the interface is then given by:

$$\vec{n} = \begin{pmatrix} y'(s) \\ -x'(s) \end{pmatrix}, \quad (14)$$

and the curvature κ can be found via

$$\kappa = \frac{x'y'' - y'x''}{(x'^2 + y'^2)^{\frac{3}{2}}}. \quad (15)$$

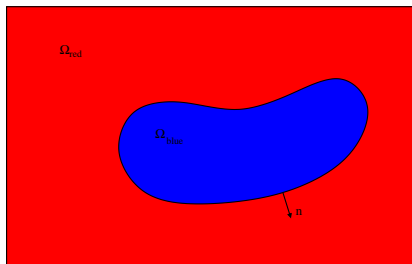


Figure 1: The two dimensional domain Ω with the red fluid occupying the region Ω_{red} and the blue fluid occupying the region Ω_{blue} . The common boundary of Ω_{red} and Ω_{blue} separates both fluids and is called the interface. At each point of the interface a normal \vec{n} can be defined. We define the normal to point into the red domain. In this case where a blue drop is enclosed by red fluid this implies that we transverse the interface of the drop in counter clockwise direction.

3. Interpolation by periodic B-Splines

As mentioned above, instead of representing the interface position directly by B-splines, as for instance done in [25] in the framework of front-tracking methods or in [12] for the volume of fluid method, we represent the interface by the two functions α , resp. β , equations (5) resp. (6), defined on the interval $[0, 2\pi]$. We use a uniform discretization of the interval $[0, 2\pi]$, meaning that we choose $N + 1$ knots $s_i \in [0, 2\pi]$:

$$s_i = \frac{2\pi i}{N}, \quad i = 0, \dots, N, \quad (16)$$

dividing the interval $[0, 2\pi]$ into N sections of equal length. Periodic B-splines can actually handle more flexible discretizations, which could be used to distribute points to regions of interest. However, in the present discussion we restrict us to the uniform case. Having now the knots s_i , $i = 0, \dots, N$, the periodic basis spline B_i^P of order P is obtained recursively by, see for instance [13, 15]:

$$B_i^P(s) = \left(\frac{s - s_i}{s_{i+P} - s_i} \right) B_i^{P-1}(s) + \left(\frac{s_{i+P+1} - s}{s_{i+P+1} - s_{i+1}} \right) B_{i+1}^{P-1}(s) \quad (17)$$

$$B_i^0(s) = \begin{cases} 1, & s_i < x \leq s_{i+1}, \\ 0, & \text{otherwise.} \end{cases} \quad (18)$$

The basis spline B_i^P has finite support $[s_i, s_{i+P+1}]$. Therefore representing the function $f(s)$ to interpolate as a linear combination $R(s)$ of the periodic basis splines B_i^P :

$$f(s) \approx R(s) = \sum_{i=-P}^{N-P-1} c_i B_i^P(s), \quad (19)$$

leads to a cyclic banddiagonal system with bandwidth P for the unknown coefficients c_i . In the present discussion we will only use odd order B-splines. The function values f_i for interpolation are then taken at the knots s_i [15]:

$$f_i = f(s_i). \quad (20)$$

For the resulting interpolation we have the following bound, see for instance [13]. If $f \in \mathcal{C}^{P+1}([0, 2\pi])$ and if f and the interpolating spline R of order P are periodic on $[0, 2\pi]$, the following bound holds:

$$\|f - R\|_{L^2} \leq C^2(P) h^{P+1} \|f\|_{H^{P+1}}, \quad (21)$$

where $h = \max_{1 \leq i \leq N-1} (s_i - s_{i-1})$ and the constant C is given by:

$$C(P) = 2^{-\frac{3}{4}(P+1)-1} \left(\frac{P+1}{2} + 2 \right)!. \quad (22)$$

This implies that if choosing B-splines of order P the interpolation will have an order of accuracy $P + 1$ with respect to the grid spacing. The cyclic banddiagonal system resulting from (19) can be solved efficiently by means of a banddiagonal solver in combination with the Woodbury formula [16].

The function β , equation (6), is periodic and can thus directly be interpolated by periodic B-splines. However, the function α is not periodic but takes different values at the right and left boundary of the interval $[0, 2\pi]$:

$$\alpha(0) = 0 \quad \alpha(2\pi) = V, \quad (23)$$

where V is the area of the drop. The derivative α' is, however, periodic. In order to use periodic B-splines to interpolate the function α , we define a periodic function α^* by:

$$\alpha^*(s) = \alpha(s) - \frac{V}{2\pi}s, \quad (24)$$

which is then interpolated using periodic B-splines. Once we have an approximation to the functions α , resp. β , equations (5) resp. (6), we evaluate the integrals

$$A(s_0, s) := \int_{s_0}^s a(s') ds' \quad (25)$$

$$B(s_0, s) := \int_{s_0}^s b(s') ds', \quad (26)$$

from equations (9), resp. (10) by Gaussian quadrature [18], in order to compute the position by means of equations (11), resp. (12). This will, however, introduce additional numerical error. A consequence of this is that

the integrals in equations (25), resp. (26), might numerically not evaluate to zero for $s_0 = 0$ and $s = 2\pi$. Therefore we determine first the total quadrature error ϵ_a , resp. ϵ_b by

$$\epsilon_a = \sum_{i=0}^{N-1} q(A, s_i, s_{i+1}), \quad (27)$$

$$\epsilon_b = \sum_{i=0}^{N-1} q(B, s_i, s_{i+1}), \quad (28)$$

$$(29)$$

where the symbol $q(A, s_i, s_{i+1})$ means taking the numerical quadrature of the integral A , equation (25), from s_i to s_{i+1} . Since B-splines are discontinuous in the P^{th} derivative across the knots s_i , we perform a Gaussian quadrature on each subinterval $[s_i, s_{i+1}]$. In order to assure that the position, given by equations (11), resp. (12) is itself a periodic function of s we replace the argument a , resp. b of the integrals in equations (25), resp. (26) by a^* and b^* defined the following way:

$$a^*(s) = a(s) - \frac{\epsilon_a}{2\pi}, \quad (30)$$

$$b^*(s) = b(s) - \frac{\epsilon_b}{2\pi}. \quad (31)$$

$$(32)$$

4. Advection step

Once we are given an interface $I(t)$ at time t represented by the two functions α_t and β_t , equations (5), resp. (6), we need to formulate an advection scheme which allows to compute the interface $I(t + \Delta t)$ at time $t + \Delta t$. Before going over to the actual derivation we introduce the notions of flux and fluxing regions.

In the present discussion we assume that the flux M_{p_0,p_1} through a section with end points $p_0 = (x_0, y_0)$, resp. $p_1 = (x_1, y_1)$ can be computed for arbitrary points p_0 and p_1 . The flux M_{p_0,p_1} is given by

$$M_{p_0,p_1} = \int_t^{t+\Delta t} Q_{p_0,p_1}(t') dt' = \int_t^{t+\Delta t} \psi(x_1, y_1, t') - \psi(x_0, y_0, t') dt', \quad (33)$$

where Q is the volume flow and ψ the stream function. In the present discussion the flux M_{p_0,p_1} will be computed analytically, since we are given the analytical stream function ψ for the benchmark tests in section 5. The flux M_{p_0,p_1} has a geometrical interpretation, cf. figure 2. It can be seen as the signed area of the region of points passing through a line with end points p_0 , resp. p_1 from t to $t + \Delta t$, the fluxing region. This region is bounded by the line from p_0 to p_1 , its image at t , when tracing the line back from $t + \Delta t$ to t and the trajectories τ_0 , resp. τ_1 of the points p_0 , resp. p_1 . In order to trace a point $p = \vec{x}_0^T$ from t to $t + \Delta t$ we have to solve the following differential equation:

$$\frac{d\vec{x}}{dt} = \vec{u}(\vec{x}, t), \quad (34)$$

with initial condition \vec{x}_0 , where $\vec{u} = (-\partial_y \psi, \partial_x \psi)^T$ is the velocity field, which is for the present benchmark tests, cf. section 5, given analytically. We solve equation (34) by the classical four stage Runge-Kutta method. For the present advection scheme it is necessary to approximate the trajectory τ from time t to $t + \Delta t$ of a point $p = \vec{x}_0^T$. This is done by means of Lagrange polynomials on the Gauss Labatto Legendre (GLL) nodes, cf. for instance [18], on the interval $[t, t + \Delta t]$. If $n \geq 2$ is the number of nodes chosen, the interval $[t, t + \Delta t]$ is divided by the n GLL nodes into $n - 1$ sections δt_i , $i = 1, \dots, n - 1$. Solving equation (34) successively for each point in time

$t_j = t + \sum_{i=1}^j \delta t_i$, $j = 0, \dots, n - 1$ will give us a set of interpolation points:

$$(t_j, \vec{x}(t_j) = (x(t_j), y(t_j))^T), \quad (35)$$

where $\vec{x}(t_0) = \vec{x}_0$. The trajectory τ can then be approximated by:

$$\tau : \vec{x}(t) = \sum_{j=0}^{n-1} \vec{x}(t_j) L_j(t), \quad (36)$$

where $L_j(t)$ is the j^{th} Lagrange polynomial.

The advection step is sketched schematically in figure 3. Having the interface $I(t)$ at time t represented by the functions α_t , resp. β_t , equations (5), resp. (6), we choose a sequence of points on the interface $I(t)$, as depicted in figure 3. Several criteria might be possible according to which the points might be chosen [4]. However, in the present discussion we take the points p_j at the parameter values s_j , the nodes chosen for the discretization, equation (16). The points are computed by equations (11), resp. (12):

$$p_j = \vec{x}_j^T = \vec{x}^T(s_j) = (x(s_j), y(s_j)), \quad j = 0, \dots, N - 1. \quad (37)$$

It is known that during simulation the points on the interface can cluster in regions of the interface if always the same points on the interface are traced forward [3]. However, in the present discussion we will not treat this problem but instead focus on the general method itself.

Now that we have chosen a sequence of points $p_j(t)$ on the interface at time t , we trace $p_j(t)$ forward in time from t to $t + \Delta t$ by solving (34), as depicted in figure 3, giving us the point $p_j(t + \Delta t)$. In the following the point $p_j(t)$ at time t will be written with a tilde \tilde{p}_j to indicate that this quantity is at time t . Its image $p_j(t + \Delta t)$ at time $t + \Delta t$ will be written without tilde p_j .

Focusing now on two consecutive points p_j and p_{j+1} at time $t + \Delta$, we know that the area bounded by the interface $I(t)$ at time t , by the trajectories τ_j and τ_{j+1} of the points p_j , resp. p_{j+1} , and the interface $I(t + \Delta t)$ at time $t + \Delta t$ must equal $M_{p_j p_{j+1}}$, as depicted in figure 3. The flux $M_{p_j, p_{j+1}}$ can thus be written as a sum of integrals along the bounding lines of the fluxing region:

$$M_{p_j, p_{j+1}} = -S_{I_{t,j}} + S_{\tau_j} - S_{\tau_{j+1}} + S_{I_{t+\Delta t,j}}, \quad (38)$$

where $S_{I_{t,j}}$ is the integral along the interface $I(t)$ from s_j to s_{j+1} ,

$$S_{I_{t,j}} = \int_{s_j}^{s_{j+1}} \vec{F}(s') \cdot \vec{n}(s') ds' \quad (39)$$

$$= \alpha_t(s_{j+1}) - \alpha_t(s_j), \quad (40)$$

since we are representing the interface $I(t)$ by means of α_t and β_t , cf. equation (5), resp. (6). The integral S_τ on a trajectory τ is given by

$$S_\tau = \int_t^{t+\Delta t} \vec{F}(t') \cdot \vec{n}(t') dt' = \frac{1}{2} \sum_{k=0}^n \sum_{m=0}^n x_k y_m \int_t^{t+\Delta t} L_k(t') L'_m(t') - L'_k(t') L_m(t') dt'. \quad (41)$$

Since $L_k L'_m$ is a polynomial of order $2(n-1) - 1$ in t , Gaussian quadrature can be used to compute the integral (41) exactly. Finally the integral $S_{I_{t+\Delta t,j}}$ on the interface at time $t + \Delta t$ can be written as

$$S_{I_{t+\Delta t,j}} = \int_{s_j}^{s_{j+1}} \vec{F}(s') \cdot \vec{n}(s') ds' \quad (42)$$

$$= \alpha_{t+\Delta t}(s_{j+1}) - \alpha_{t+\Delta t}(s_j), \quad (43)$$

where $\alpha_{t+\Delta t}$ is the unknown function α representing the interface at time $t + \Delta t$. We can solve equation (38) for $\alpha_{t+\Delta t}(s_{j+1})$:

$$\alpha_{t+\Delta t}(s_{j+1}) = M_{p_j, p_{j+1}} + \alpha_t(s_{j+1}) - \alpha_t(s_j) - S_{\tau_j} + S_{\tau_{j+1}} + \alpha_{t+\Delta t}(s_j) \quad (44)$$

$$\begin{aligned}
&= \alpha_{t+\Delta t}(s_0) + \sum_{k=0}^j M_{p_k, p_{k+1}} + \alpha_t(s_{k+1}) - \alpha_t(s_k) - S_{\tau_k} + S_{\tau_{k+1}} \\
&= \alpha_t(s_{j+1}) + S_{\tau_{j+1}} - S_{\tau_0} + \sum_{k=0}^j M_{p_k, p_{k+1}}, \tag{46}
\end{aligned}$$

since we have chosen $\alpha_t(s_0) = \alpha_{t+1}(s_0) = 0$. A kind of similar idea is used for surface marker particles in order to correct for area loss during advection, cf. [25]. In the present method it is, however, not used as a correction but as the principle behind the advection step.

The interpolation points

$$(s_j, \alpha_{t+\Delta t}(s_j)), \quad \text{resp.} \quad (s_j, x_j y_j), \quad j = 0, \dots, N, \tag{47}$$

are then interpolated as mentioned in section 3 to give an interpolant of α resp. β for the interface $I(t + \Delta t)$ at time $t + \Delta t$. The area of the drop V is conserved, since $\alpha(s_N = 2\pi) = V$ for all time steps. However, this conservation property should be understood in a less strict sense, since the quadrature errors ϵ_a , resp. ϵ_b in equations (27), resp. (28) will lead to the fact that the area bounded by the actual interface given by the points computed by equations (11) and (12) can be different from V . In addition, errors can lead to the development of self intersections of the interface, cf. figure (4). Area conservation should rather be understood as the underlying principle of the method which is implemented through the function α which, together with β , can be seen as a kind of generating function for the position.

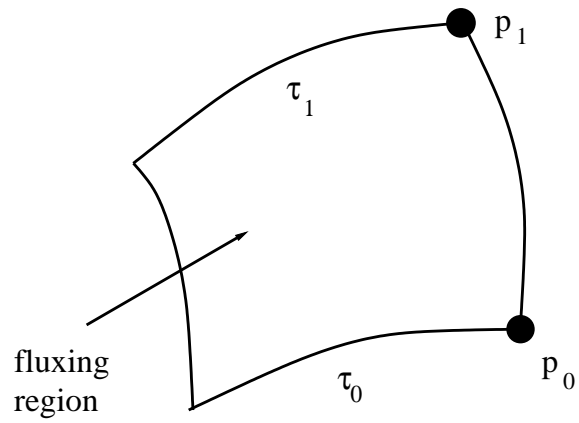


Figure 2: The fluxing region is the set of points fluxed through the line with end points p_0 , resp. p_1 , from time t to $t + \Delta t$. It is bounded by the trajectories τ_0 , resp. τ_1 of the points p_0 , resp. p_1 when tracing them back in time, the line from p_0 to p_1 and the image of this line when tracing the line back in time.

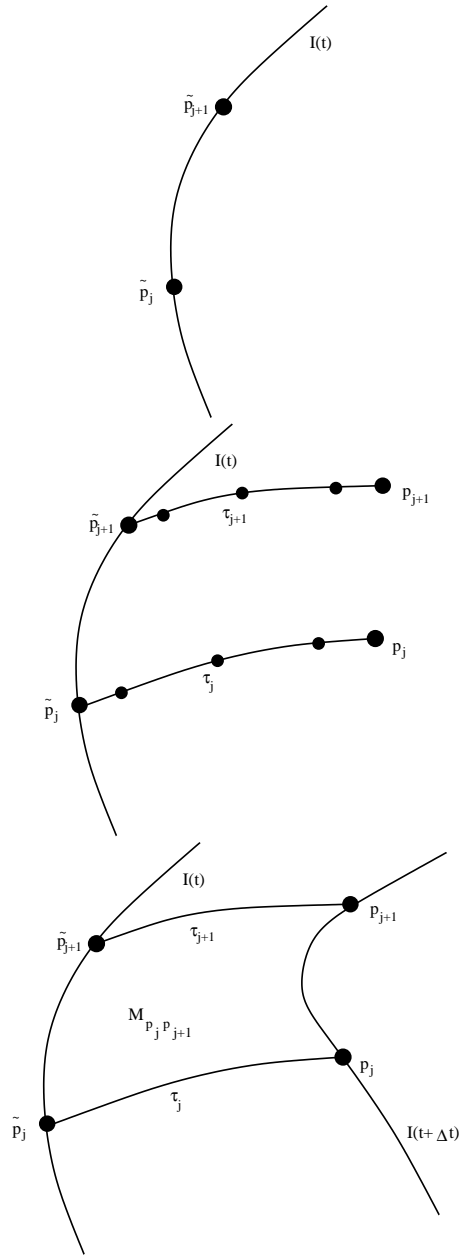


Figure 3: Sketch of the advection step. TOP: Going along the interface $I(t)$ at time t we sample a sequence of points \tilde{p}_j . MIDDLE: These points are traced forward in time along their trajectories τ_j to their positions p_j at time $t + \Delta t$. At the Gauss Labatto Legendre nodes of the interval $[t, t + \Delta t]$, we record the positions of the point p_j which are then used to find an interpolation approximating the trajectory τ_j . BOTTOM: The flux $M_{p_j, p_{j+1}}$ can be interpreted as the signed area of the region bounded by the interface $I(t)$ at time t the interface $I(t + \Delta t)$ at time $t + \Delta t$ and the trajectories τ_j and τ_{j+1} .

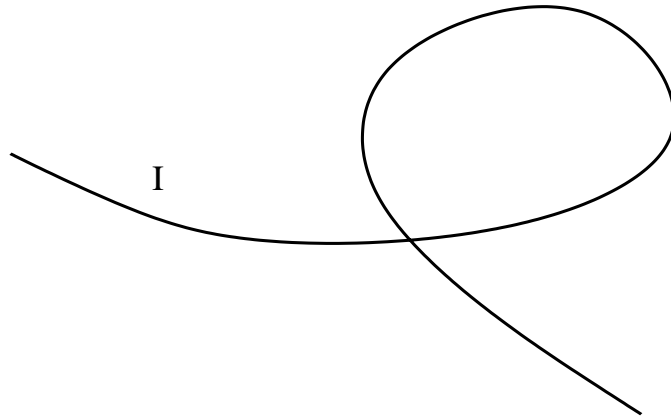


Figure 4: Self intersection of the interface. Errors can lead to self intersection of the interface.

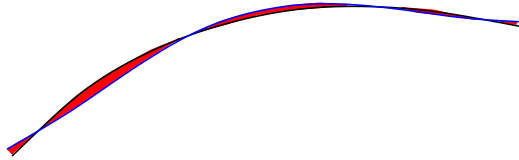


Figure 5: The error norm E_1 measures the total area (marked by red color) included between the numerical interface (marked by a blue line) and the exact interface (marked by a black line).

5. Numerical verification

The numerical verification of the present third order volume of fluid method is done by three classical benchmark tests, the reversed single vortex test by Rider and Kothe [19], Zalesak's slotted disk test [27] and the deformation field test [21]. However, before going over to the numerical verification, we have a glance at the definition of the numerical error.

5.1. Numerical Error

The error norm E in the present discussion measures the area difference between the numerical interface and the exact interface as depicted in figure 5. The error is computed using the position of the interface computed by means of equations (11), resp. (12) and not by means of the function α , equation (5). The integration between the numerical solution and the exact interface in order to compute the area difference is done by means of Gaussian quadrature, where we ensured that the quadrature error is negligible compared to the numerical error of the method. The order of convergence O between two resolutions n and $2n$, is computed using E :

$$O = \frac{\ln(E(n)/E(2n))}{\ln 2}. \quad (48)$$

5.2. Numerical verification part 1

The setup of the reversed single-vortex test of Rider and Kothe [19] consists of a circular drop of radius $r_0 = 0.15$ placed at position $(x_0, y_0) = (0.5, 0.75)$ in a unit square box. The velocity field $\vec{u} = (-\partial_y \psi, \partial_x \psi)^T$ is obtained by means of the following stream function ψ :

$$\psi(x, y, t) = \frac{1}{\pi} \cos\left(\frac{\pi t}{T}\right) \sin^2(\pi x) \sin^2(\pi y), \quad (49)$$

where T is the period at which the drop has returned to its initial position. Thereby its interface at time T should match the initial circle. The discrepancy between the numerical interface at time T and the exact circle serves as a measure of the numerical error. As initial condition we used

$$\alpha = \frac{1}{2} r_0^2 s + r_0 (x_0 \sin s - y_0 \cos s + y_0) \quad (50)$$

$$\beta = (r_0 \cos s + x_0) (r_0 \sin s + y_0), \quad (51)$$

where $s \in [0, 2\pi]$. As mentioned in section 3, we divided $[0, 2\pi]$ into N equidistant sections. We performed three series of tests for $T = 1/2$, $T = 2$ and $T = 8$. The results of these tests are shown in figures 6, 7, 8,9, 10,11,12, 13,14, 15,16 and tables 1, 2, 3. For all simulations we chose $n = 5$ for the approximation of the trajectories for the advection step, cf. section 4. Depending on the order P of the B-spline interpolation we chose a different value for the time steps Δt in order to make the error contribution due to the advection step subdominant compared to the error contribution of the interface Reconstruction. The advection step itself can handle quite large time steps without displaying any sign of instability. All simulations were performed using B-splines of order $P = 3, 5, 7$. For $P = 3$ the time step was

chosen $\Delta t = 1/32$, for $P = 5$, $\Delta t = 1/128$, and for $P = 7$, $\Delta t = 1/256$. The time step was kept fixed at these values even when going over to finer resolutions. In figure 6 the resulting position of the interface is shown for $t = T/2$ and $t = T$ in the case $T = 1/2$, $P = 3$ and a resolution of $N = 10$. The interface is well resolved and does not display any visual disturbances such as bumps or oscillations at maximum deformation and when it has returned to its initial position at $t = T$. The same observation can be made for the case $T = 2$, cf. figure 8. Concerning the convergence of the method for these two cases, e.g. $T = 1/2$ and $T = 2$, cf. figures 7, resp. 9 and tables 1, resp. 2, we observe that the order of convergence corresponds approximately to the theoretical value of $P + 1$, cf. equation (21). For $P = 7$ and fine resolutions the error does not further decrease because of the round off limit. In addition, for the case $T = 2$ when going from $N = 20$ to $N = 40$, we observe a sudden jump in the convergence, cf. figure 9 and table 2, for $P = 5$ and $P = 7$. This phenomenon of accelerated convergence is even more pronounced in the case $T = 8$, cf. figure 12 and table 3. An explanation for this sudden increase in convergence might lie in a underresolution of the problem for coarse resolutions N , meaning that when increasing P , keeping N fixed at a small value no important gain in accuracy is observed. However, if the resolution is finer, i.e. large values of N , increasing P will almost lead to spectral convergence, i.e. faster than algebraic. This points to the eventuality of having insufficient sampling of the signal, i.e. an aliasing error. This is different to classical spectral methods such as methods based on Chebyshev or Legendre polynomials for which increasing the approximation order introduces an increase of spatial resolution by increasing the number of Gauss

points. Periodic B-splines on the contrary offer the possibility of increasing P and N independently with the consequence of having eventually a persisting aliasing error when only increasing P . Even worse a underresolved simulation can lead to an entirely wrong solution by the present method, as can be seen in figure 10. Here $T = 8$ and the resolution N was fixed at 20 ($P = 3$). For $t = T/2$ still a few structures of the correct solution are recognizable, however for $t = T$ the picture has entirely deteriorated. If underresolved, the numerical solution can display self intersections. This indicates that the present method is less robust to underresolution. However, for well resolved cases, which for the case $T = 8$ start at only 40 knots, cf. figure 11, the present numerical scheme produces a very accurate result.

Concerning area conservation, we observe from figure 13 that the value $\alpha(2\pi)$ is, apart from round off contributions, equal to the initial area of the drop. However, the quadrature errors ϵ_a , resp. ϵ_b , equations (27), resp. (28), can become rather important during simulation, as for instance for the underresolved case $T = 8$, $N = 20$ and $P = 3$, cf. figure 14, indicating a possible discrepancy between the actual area of the drop and $\alpha(2\pi)$. For well resolved cases the quadrature errors are smaller, cf. figure 15, but seem to increase with increasing deformation of the drop.

As a last numerical experiment we investigated the accuracy of the advection scheme derived in section 4. By fixing the number of Gauss Labatto Legendre nodes to $n = 5$, the interpolating polynomial has order 4 for which reason we expect the advection scheme to converge with 5th order accuracy with respect to the time step Δt . In order to observe the error contribution by the advection scheme, we chose a B-spline of order $P = 7$ and a spa-

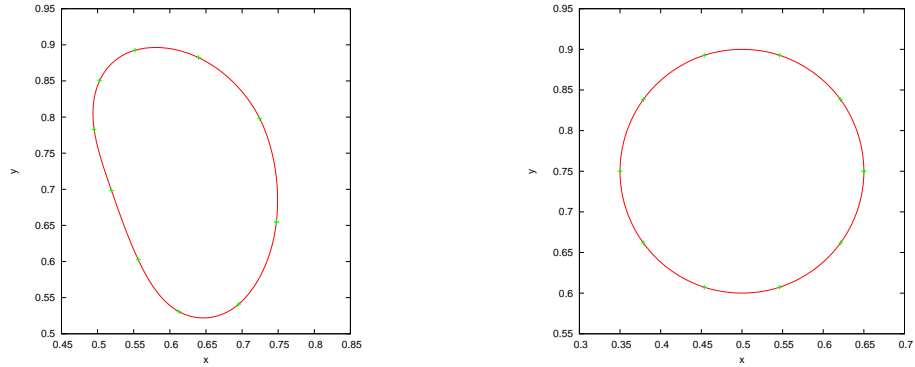


Figure 6: Result of the Rider-Kothe single vortex benchmark test for $T = 1/2$. The resolution was $N = 10$ and $P = 3$. LEFT: Position of the interface at $t = T/2$. RIGHT: Position of the interface at $t = T$.

tial resolution of $N = 160$, such that the error contribution by the interface representation is subdominant. Decreasing the time step Δt leads indeed to a fifth order convergence of the numerical error up to the point at which the error contribution by the interface representation becomes dominant, cf. figure 16.

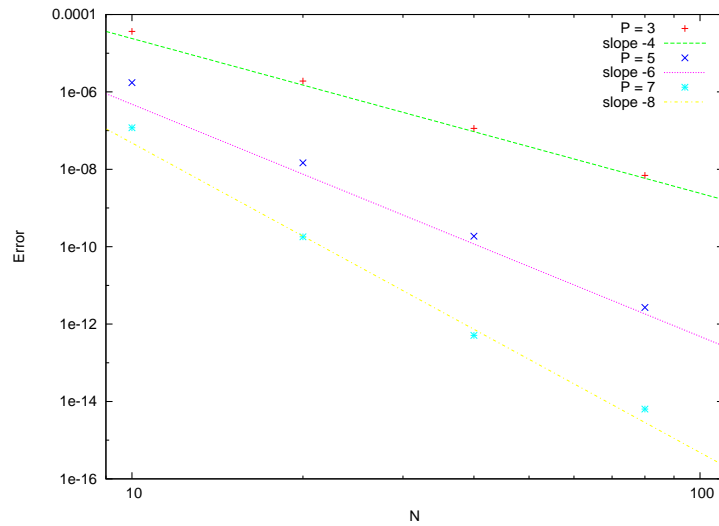


Figure 7: Error decrease for the Rider-Kothe single vortex benchmark test for $T = 1/2$, for increasing resolution N using B-splines of different order P .

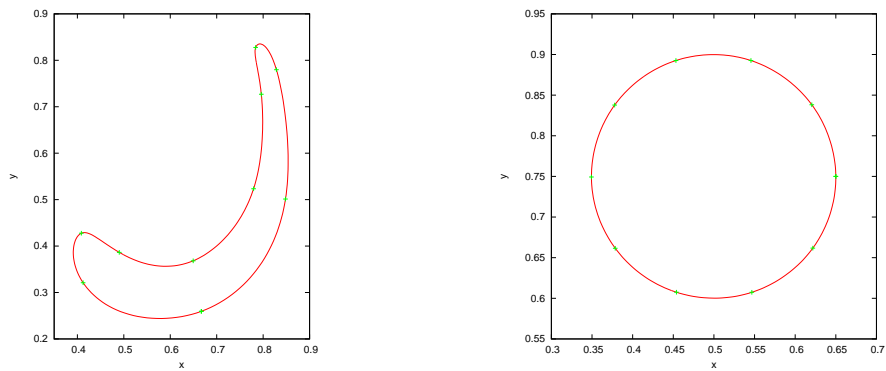


Figure 8: Result of the Rider-Kothe single vortex benchmark test for $T = 2$. The resolution was $N = 10$ and $P = 3$. LEFT: Position of the interface at $t = T/2$. RIGHT: Position of the interface at $t = T$.

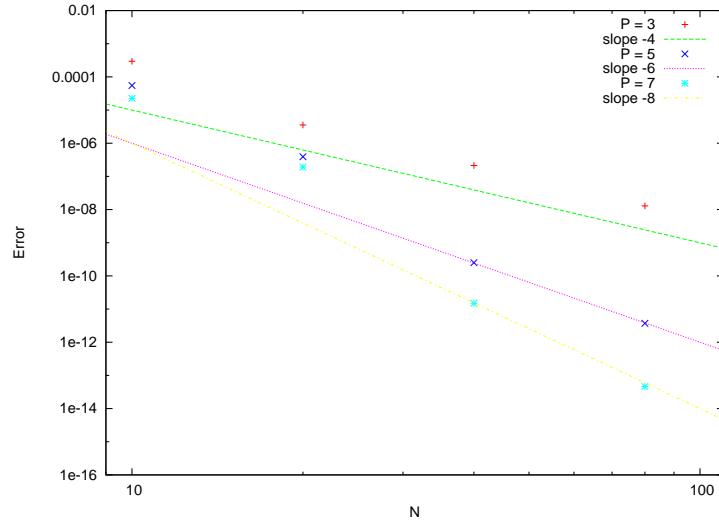


Figure 9: Error decrease for the Rider-Kothe single vortex benchmark test for $T = 2$, for increasing resolution N using B-splines of different order P .

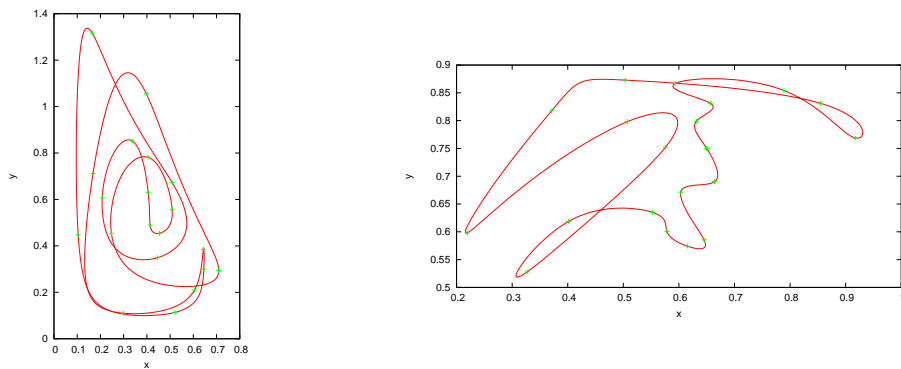


Figure 10: Result of the Rider-Kothe single vortex benchmark test for $T = 8$. The resolution was $N = 20$ and $P = 3$. LEFT: Position of the interface at $t = T/2$. RIGHT: Position of the interface at $t = T$. In this case the resolution chosen was too coarse leading to a break down of the present method.

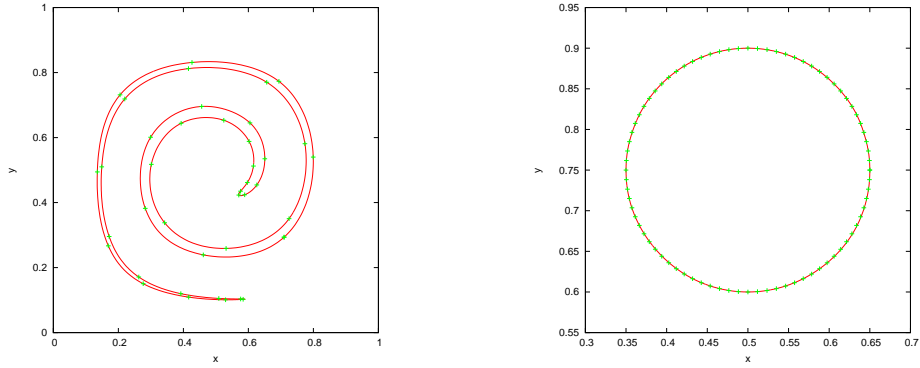


Figure 11: Result of the Rider-Kothe single vortex benchmark test for $T = 8$. The resolution was $N = 40$ and $P = 3$. LEFT: Position of the interface at $t = T/2$. RIGHT: Position of the interface at $t = T$.

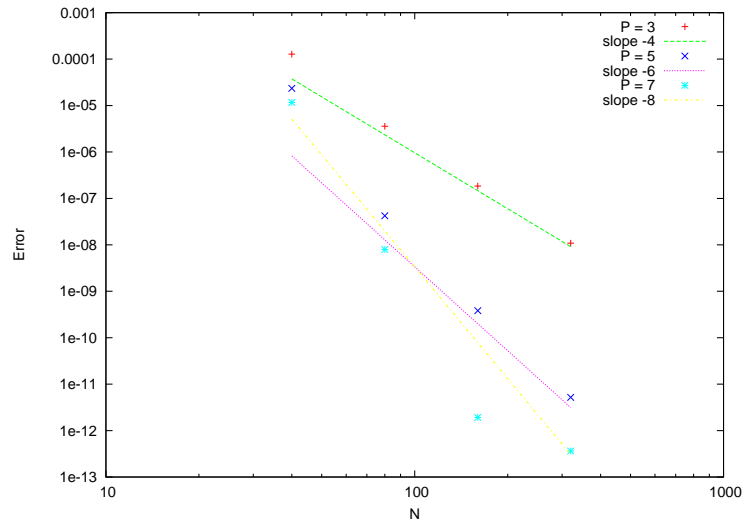


Figure 12: Error decrease for the Rider-Kothe single vortex benchmark test for $T = 8$, for increasing resolution N using B-splines of different order P .

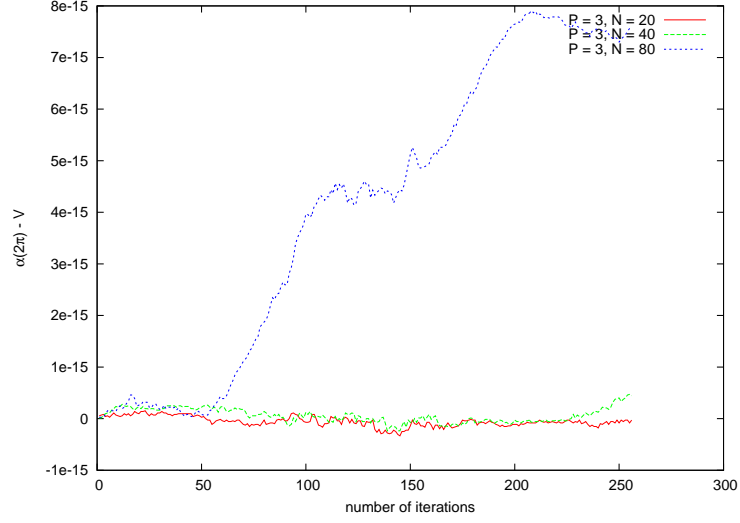


Figure 13: The difference of the exact area V of the drop to the area of the drop given by $\alpha(2\pi)$ during the Rider-Kothe single vortex benchmark test for $T = 8$.

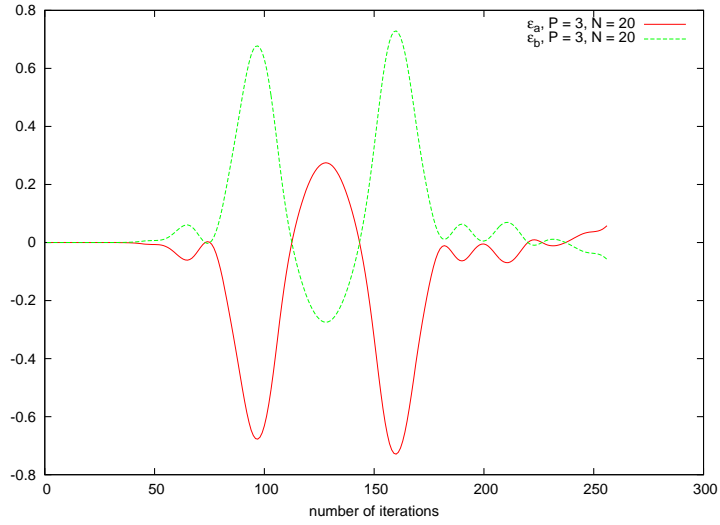


Figure 14: The quadrature errors ϵ_a , resp. ϵ_b , defined in equations (27), resp. (28) during the Rider-Kothe single vortex benchmark test for $T = 8$. The corresponding position of the interface is displayed in figure 10 at some instances in time. For this low resolution ($N = 20$, $P = 3$) the method breaks down. This is also indicated by large quadrature errors meaning that the actual position of the interface, computed by means of equations (11), resp. (12), includes a large deviation from the exact position given by α and β .

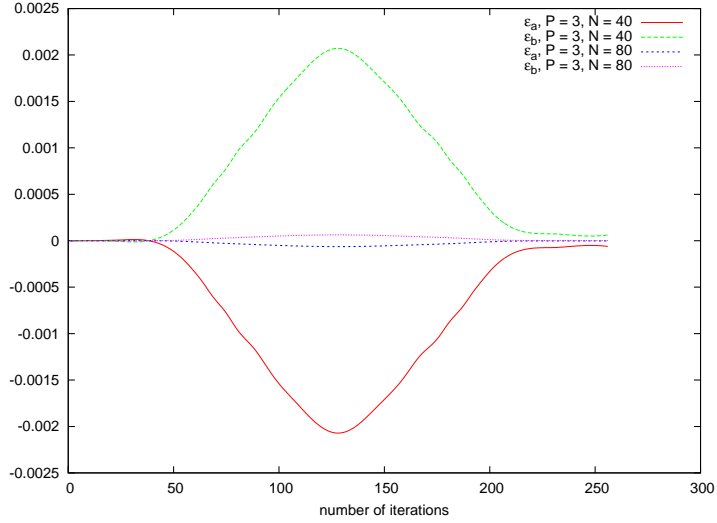


Figure 15: The quadrature errors ϵ_a , resp. ϵ_b , defined in equations (27), resp. (28) during the Rider-Kothe single vortex benchmark test for $T = 8$. This time the resolution is sufficient ($N = 40, 80$, $P = 3$) which is also indicated by a smaller quadrature error compared to the one in figure 14. For maximum deformation of the drop we are confronted with a maximum quadrature error.

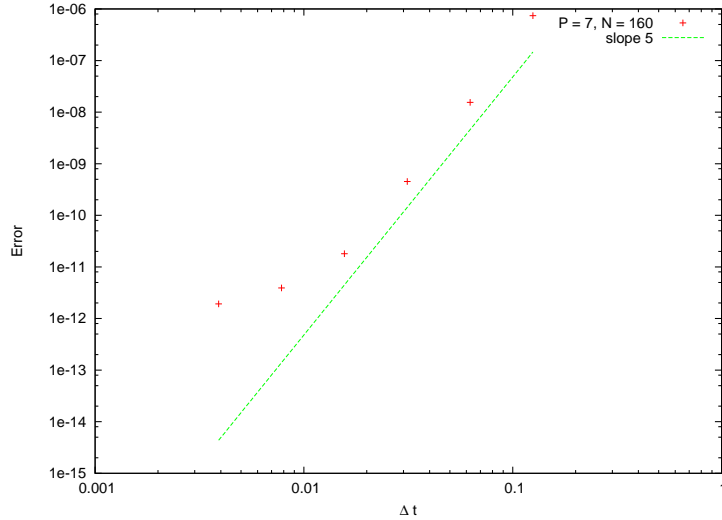


Figure 16: Error increase for the Rider-Kothe single vortex benchmark test for $T = 8$, for increasing time step Δt using B-splines of order $P = 7$ and a resolution of $N = 160$.

P	N	Error	O
3	10	3.66583×10^{-5}	—
	20	1.91077×10^{-6}	4.26
	40	1.14024×10^{-7}	4.07
	80	6.96072×10^{-9}	4.03
5	10	1.74018×10^{-6}	—
	20	1.47129×10^{-8}	6.87
	40	1.87246×10^{-10}	6.30
	80	2.69292×10^{-12}	6.12
7	10	1.18328×10^{-7}	—
	20	1.79321×10^{-10}	9.37
	40	5.09673×10^{-13}	8.46
	80	6.38136×10^{-15}	6.32

Table 1: Results for the Rider-Kothe single vortex benchmark test for $T = 1/2$

P	N	Error	O
3	10	2.96591×10^{-4}	—
	20	3.54562×10^{-6}	6.39
	40	2.13069×10^{-7}	4.06
	80	1.29146×10^{-8}	4.04
5	10	5.50018×10^{-5}	—
	20	3.90107×10^{-7}	7.14
	40	2.51014×10^{-10}	10.60
	80	3.72075×10^{-12}	6.08
7	10	2.25578×10^{-5}	—
	20	1.91445×10^{-7}	6.88
	40	1.49644×10^{-11}	13.64
	80	4.62276×10^{-14}	8.33

Table 2: Results for the Rider-Kothe single vortex benchmark test for $T = 2$

P	N	Error	O
3	40	1.28241×10^{-4}	—
	80	3.57649×10^{-6}	5.16
	160	1.84163×10^{-7}	4.30
	320	1.08844×10^{-8}	4.08
5	40	2.34006×10^{-5}	—
	80	4.21891×10^{-8}	9.12
	160	3.82007×10^{-10}	6.79
	320	5.19595×10^{-12}	6.20
7	40	1.16624×10^{-5}	—
	80	7.93665×10^{-9}	10.52
	160	1.92373×10^{-12}	12.01
	320	3.63856×10^{-13}	2.40

Table 3: Results for the Rider-Kothe single vortex benchmark test for $T = 8$

5.3. Numerical verification part 2

The slotted disk rotation test of Zalesak [27] uses a solid body rotation to advect a slotted disk. The stream function ψ is given by

$$\psi(x, y) = \frac{\omega}{2} \{(x - x_0)^2 + (y - y_0)^2\}, \quad (52)$$

where ω is chosen in such a way as to allow a complete rotation of the drop in 2524 iterations. The computational box is four by four and the drop has a radius of $r_0 = 1/2$. It is situated at $(x_0, y_0) = (2, 2.75)$. The coordinates of the four corners of the slot are given by:

$$(x_a, y_a) = \left(x_0 + \frac{3}{50}, y_0 - \sqrt{r_0^2 - (x_a - x_0)^2}\right) \quad (53)$$

$$(x_b, y_b) = \left(x_a, y_0 + \frac{5}{50}\right) \quad (54)$$

$$(x_c, y_c) = \left(x_0 - \frac{3}{50}, y_b\right) \quad (55)$$

$$(x_d, y_d) = (x_c, y_a). \quad (56)$$

As an initial condition we chose a description of the initial interface by means of four functions $\alpha_1, \alpha_2, \alpha_3, \alpha_4$, defined the following way:

$$\alpha_1(s) = \frac{1}{2} \left(r_0^2 s - r_0 (x_0 (\cos(s + s_a) - \cos(s_a)) + y_0 (\sin(s + s_a) - \sin(s_a))) \right) \quad (57)$$

$$\alpha_2(s) = \frac{1}{2} x_c s, \quad (58)$$

$$\alpha_3(s) = -\frac{1}{2} y_b s, \quad (59)$$

$$\alpha_4(s) = \frac{1}{2} x_a s, \quad (60)$$

$$(61)$$

where $s_a = \arcsin\left(\frac{x_a - x_0}{r_0}\right)$ and $s_b = \arcsin\left(\frac{x_0 - x_c}{r_0}\right)$. The function α is composed by means of these four functions.

$$\alpha(s) = \begin{cases} \alpha_1(s) & 0 < s \leq 2\pi - s_b - s_a \\ \alpha_2(s - 2\pi + s_b + s_a) & 2\pi - s_b - s_a \\ \quad + \alpha_1(2\pi - s_b - s_a) & < s \leq 2\pi - s_b - s_a + y_b - y_a \\ \alpha_3(s - 2\pi + s_b + s_a - y_b + y_a) & 2\pi - s_b - s_a + y_b - y_a \\ \quad + \alpha_2(y_b - y_a) & < s \\ \quad + \alpha_1(2\pi - s_b - s_a) & \leq 2\pi - s_b - s_a + y_b - y_a + x_a - x_c \\ \alpha_4(2\pi - s_b - s_a + y_b - y_a + x_a - x_c - s) & 2\pi - s_b - s_a + y_b - y_a + x_a - x_c \\ \quad + \alpha_3(x_a - x_c) & < s \\ \quad + \alpha_2(y_b - y_a) & \leq 2\pi - s_b - s_a + 2(y_b - y_a) + x_a - x_c \\ \quad + \alpha_1(2\pi - s_b - s_a) & \end{cases} \quad (62)$$

The parameter s takes values in the interval $[0, 2\pi - s_b - s_a + 2(y_b - y_a) + x_a - x_c]$ this time. We discretized this interval in such a way that the corner positions of the slot are at knots of the discretization. The function α is then interpolated at these knots. The function β is handled likewise, with β given

by:

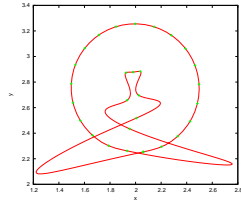
$$\beta(s) = \begin{cases} (r_0 \sin(s + s_a) + x_0) & 0 < s \leq 2\pi - s_b - s_a \\ (-r_0 \cos(s + s_a) + y_0) & \\ x_d(y_a + s - 2\pi + s_b + s_a) & 2\pi - s_b - s_a \\ & < s \leq 2\pi - s_b - s_a + y_b - y_a \\ y_b(x_d + s - 2\pi + s_b + & 2\pi - s_b - s_a + y_b - y_a \\ & < s \\ s_a - y_b + y_a + x_d) & \leq 2\pi - s_b - s_a + y_b - y_a + x_a - x_c \\ x_a(y_b - s + 2\pi - s_b - & 2\pi - s_b - s_a + y_b - y_a + x_a - x_c \\ & < s \\ s_a + y_b - y_a + x_a - x_c) & \leq 2\pi - s_b - s_a + 2(y_b - y_a) + x_a - x_c. \end{cases} \quad (63)$$

The initial condition is only C^0 because of the kinks at the corners of the slot. Although using high order periodic B-splines, we expect the convergence rate therefore to be of only second order at most. In addition, discontinuities can give rise to the development of spurious oscillations of the interpolant at these discontinuities, the so called Gibbs phenomenon [5]. The higher the order of the periodic B-splines the further these spurious oscillations spread along the interface, as can be seen when comparing figures 17 and 18, where we compare the interface position at time $t = 0$ and $t = T$, after one rotation, for different resolutions. Intermediate steps are shown for $N = 160$ and $P = 3$ in figure 19, indicating that the main contribution to the overall error does indeed not come from the advection but from the interpolation of a function with discontinuities in its first derivative. The order of convergence is reduced to second order no matter the order of the B-spline interpolation, cf. figure

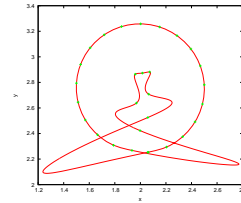
P	N	Error	O
1	28	2.03638×10^{-2}	–
	56	5.10861×10^{-3}	1.99
	112	1.27831×10^{-3}	2.00
	224	3.19646×10^{-4}	2.00
	448	7.99148×10^{-5}	2.00
3	28	3.82303×10^{-1}	–
	56	6.76916×10^{-2}	2.50
	112	1.58615×10^{-2}	2.09
	224	4.25359×10^{-3}	1.90
	448	1.08273×10^{-3}	1.94
5	28	3.76212×10^0	–
	56	2.40403×10^{-1}	3.97
	112	4.16235×10^{-2}	2.53
	224	9.12356×10^{-3}	2.19
	448	2.12014×10^{-3}	2.11

Table 4: Results for Zalesak’s slotted disk rotation test for $P = 3$ and $P = 5$.

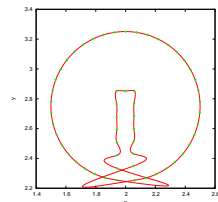
20, resp. table 4. The absolute error is even larger for higher order B-spline interpolation, due to the larger spurious oscillations. We remark that choosing an order $P = 1$ for the B-spline interpolation gives us a PLIC like description of the interface, which for the present benchmark test produces more accurate results since it only requires \mathcal{C}^0 continuity of the function to be interpolated. This leads to the result that for $P = 1$ the slot stays sharp during the entire simulation as can be seen in figure 21.



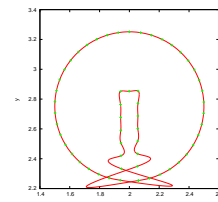
$N = 28, t = 0$



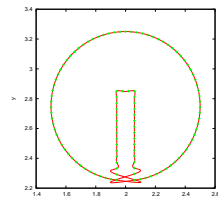
$N = 28, t = T$



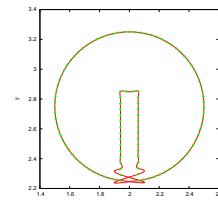
$N = 56, t = 0$



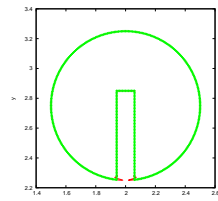
$N = 56, t = T$



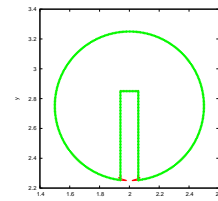
$N = 112, t = 0$



$N = 112, t = T$

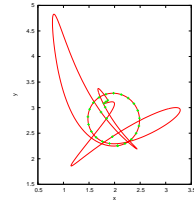


$N = 448, t = 0$

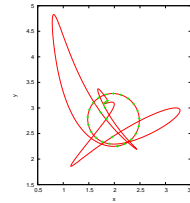


$N = 448, t = T$

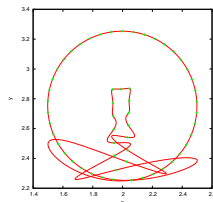
Figure 17: Result of Zalesak's slotted disk rotation test for different resolutions N . The order of B-spline interpolation is $P = 3$. Shown are the graphs at the initial position, $t = 0$, and the position after a full rotation, $t = T$.



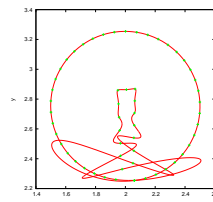
$N = 28, t = 0$



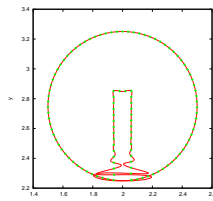
$N = 28, t = T$



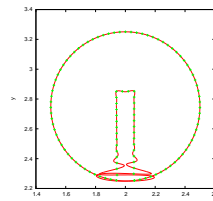
$N = 56, t = 0$



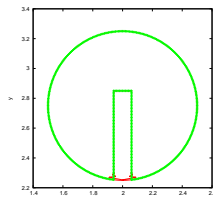
$N = 56, t = T$



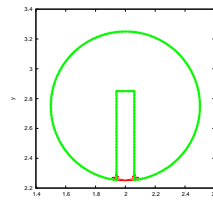
$N = 112, t = 0$



$N = 112, t = T$



$N = 448, t = 0$



$N = 448, t = T$

Figure 18: Result of Zalesak's slotted disk rotation test for different resolutions N . The order of B-spline interpolation is $P = 5$. Shown are the graphs at the initial position, $t = 0$, and the position after a full rotation, $t = T$.

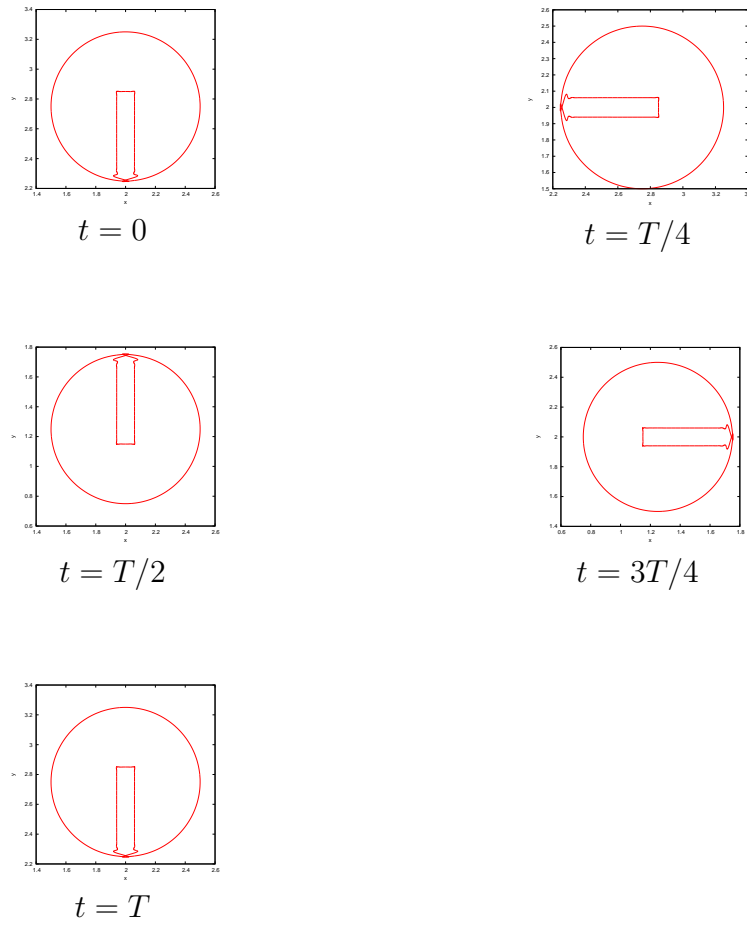


Figure 19: Result of Zalesak's slotted disk rotation test for $N = 224$ and $P = 3$. The graphs are shown at different points in time.

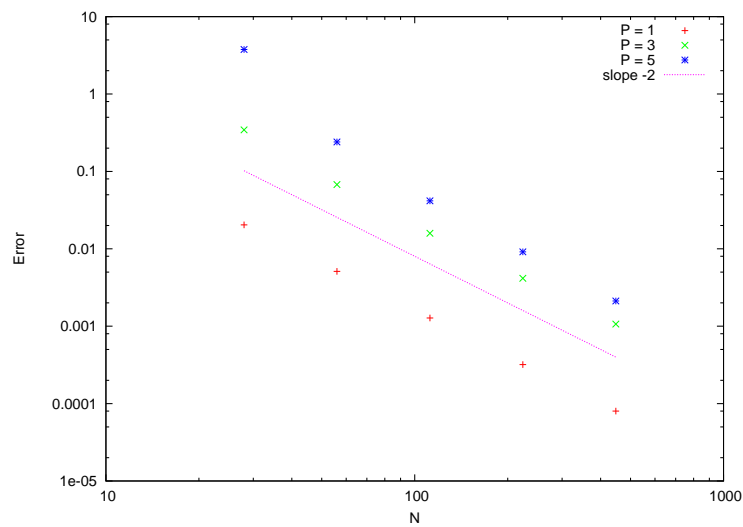


Figure 20: Error decrease for Zalesak's slotted disk rotation test. Due to the discontinuity in the first derivative of the solution, the present method exhibits only second order accuracy with respect to the resolution N . In addition, the fifth order B-spline interpolation is less accurate than the third order one, since the spurious oscillations are larger in the former case.

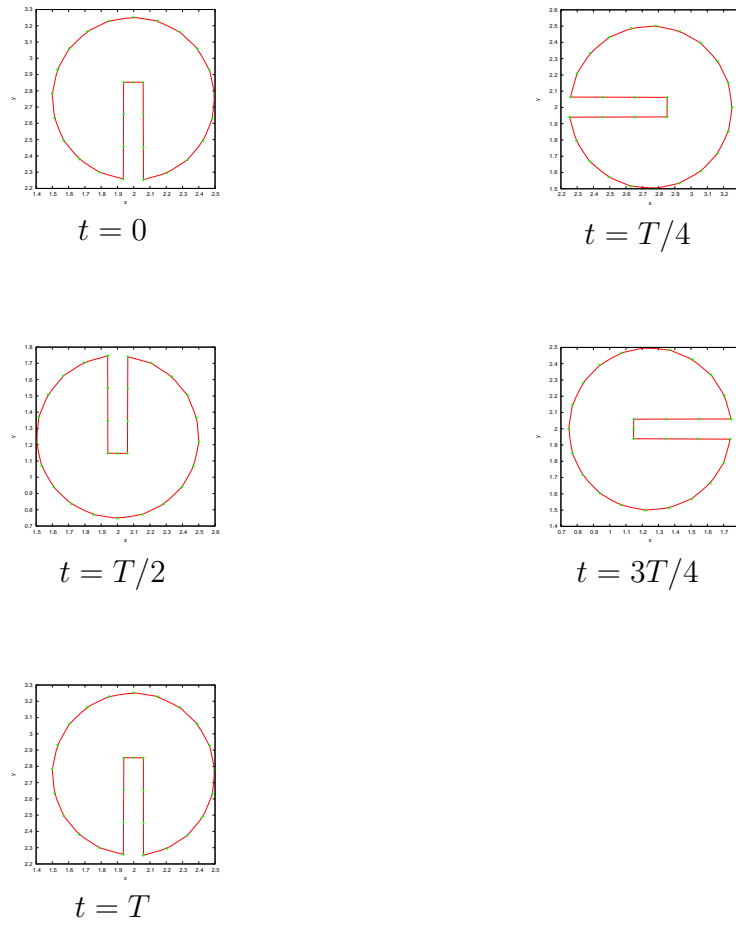


Figure 21: Result of Zalesak's slotted disk rotation test for $N = 28$ and $P = 1$. The graphs are shown at different points in time.

5.4. Numerical verification part 3

The deformation field test [21] uses the following stream function:

$$\psi(x, y, t) = \frac{1}{n\pi} \cos\left(\frac{\pi t}{T}\right) \sin\left(n\pi\left(x + \frac{1}{2}\right)\right) \cos\left(n\pi\left(y + \frac{1}{2}\right)\right), \quad (64)$$

where n is the number of vortexes in the computation domain and chosen to be $n = 4$ to match the geometry used in [28, 24], as was the period with $T = 2$. The computational domain is a square box of side length one. A drop of radius $r_0 = 0.15$ has its center at $(x_0, y_0) = (0.5, 0.5)$ at time $t = 0$. Since the flow is reversed after $T/2$ the drop returns to its initial position at $t = T$ assuming its initial shape. As initial condition we used the same functions α , resp. β , as for the Rider-Kothe single vortex test, equations (50-51). We performed a series of tests with $P = 1$, $P = 3$ and $P = 5$. The time steps were chosen $\Delta t = 3.906 \times 10^{-3}$ for $P = 1$ and $P = 3$ and $\Delta t = 9.76 \times 10^{-4}$ for $P = 4$. This was, as before, done in order to make the error contribution by the advection step subdominant. This benchmark test is relatively difficult since the interface develops regions with very small local radii of curvature. In addition, at some parts the drop becomes very thin. The results of the present method applied on this benchmark test can be seen in figures 22 for $P = 1$, 23 for $P = 3$, and 24 for $P = 5$. In these figures we depicted the graph of the interface at maximum deformation $t = T/2$ and after the drop has returned to its initial position at $t = T$ for different resolutions. For low resolutions the graph at maximum deformation ($t = T/2$) does only capture the coarse features of the solution for all three orders $P = 1$, $P = 3$ and $P = 5$. In addition, at regions where the resolution is low but the curvature high, the numerical solution seems to develop a kind of Gibbs phenomenon

for $P = 3$ and $P = 5$, as for Zalesak's slotted disk rotation test. These oscillations become smaller as the resolution increases. When the drop has returned to its initial position we observe that the interface develops spikes at those regions where the resolution was low at maximum deformation. This is due to the fact that as the error is larger in these regions a point might fall into the wrong vortex and be traced to a different location. These spikes become smaller with increasing resolution N and increasing order of the interpolating B-spline P . For finer resolutions, $N = 1250$, the final position is extremely close to the exact solution. However, at maximum deformation some wiggles can be observed for both $P = 3$ and $P = 5$, indicating that measuring the error at maximum deformation might give a better estimate of the accuracy of the present method than measuring it at the final position. For $N = 5000$ and $P = 5$ the wiggles have disappeared, as can be observed from figure 25. Concerning the order of convergence, cf. figure 26 and table 5, the present method seems to converge at a lower speed both for $P = 3$ and for $P = 5$. This might have its origin in the spurious oscillations which might prevent the method from converging at the right rate. Grid adaptation or remeshing redistributing the points to regions were needed, as mentioned in section 3, might be advantageous for this benchmark test. Nevertheless, an order of convergence between three and four with respect to the spatial resolution for this benchmark test is quite acceptable.

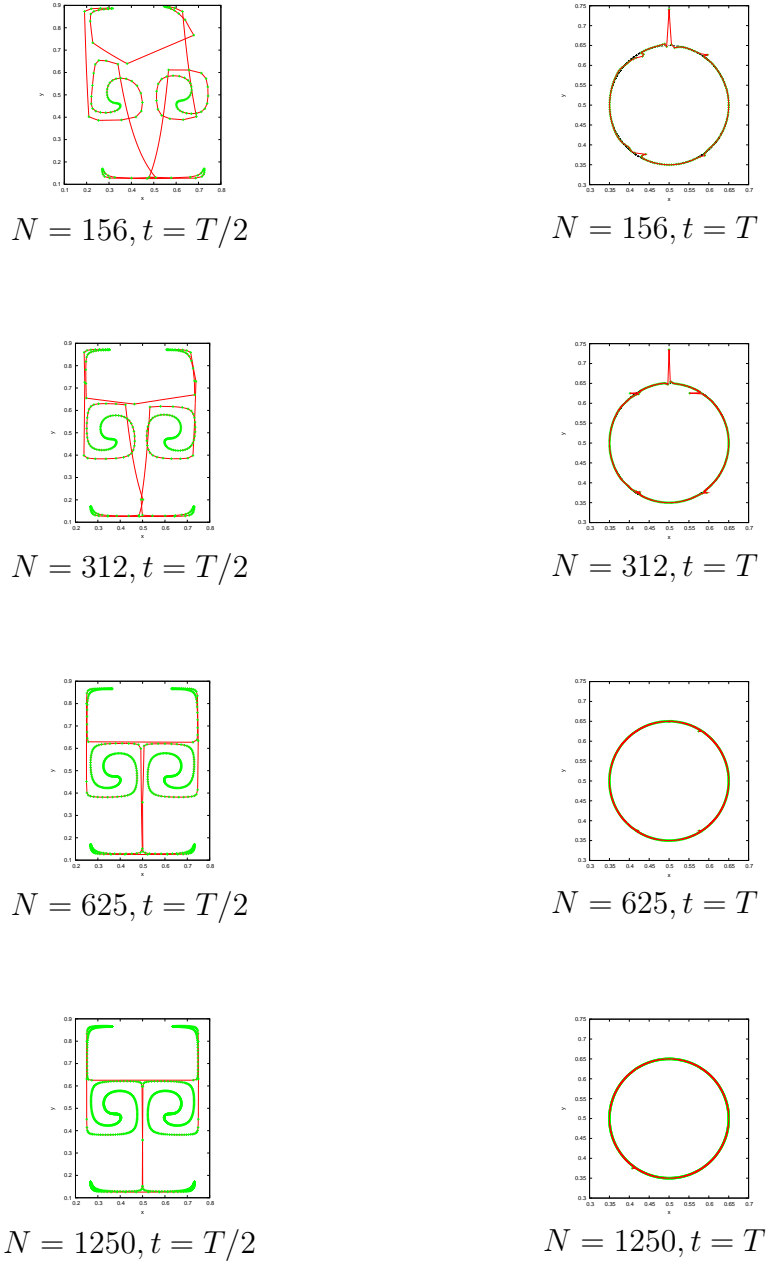


Figure 22: Result of the deformation field test for different resolutions N . The order of B-spline interpolation is $P = 1$. The graphs are shown at the maximal deformation, $t = T/2$ and after returning to the initial position $t = T$. The black dashed line is the exact solution for $t = T$.

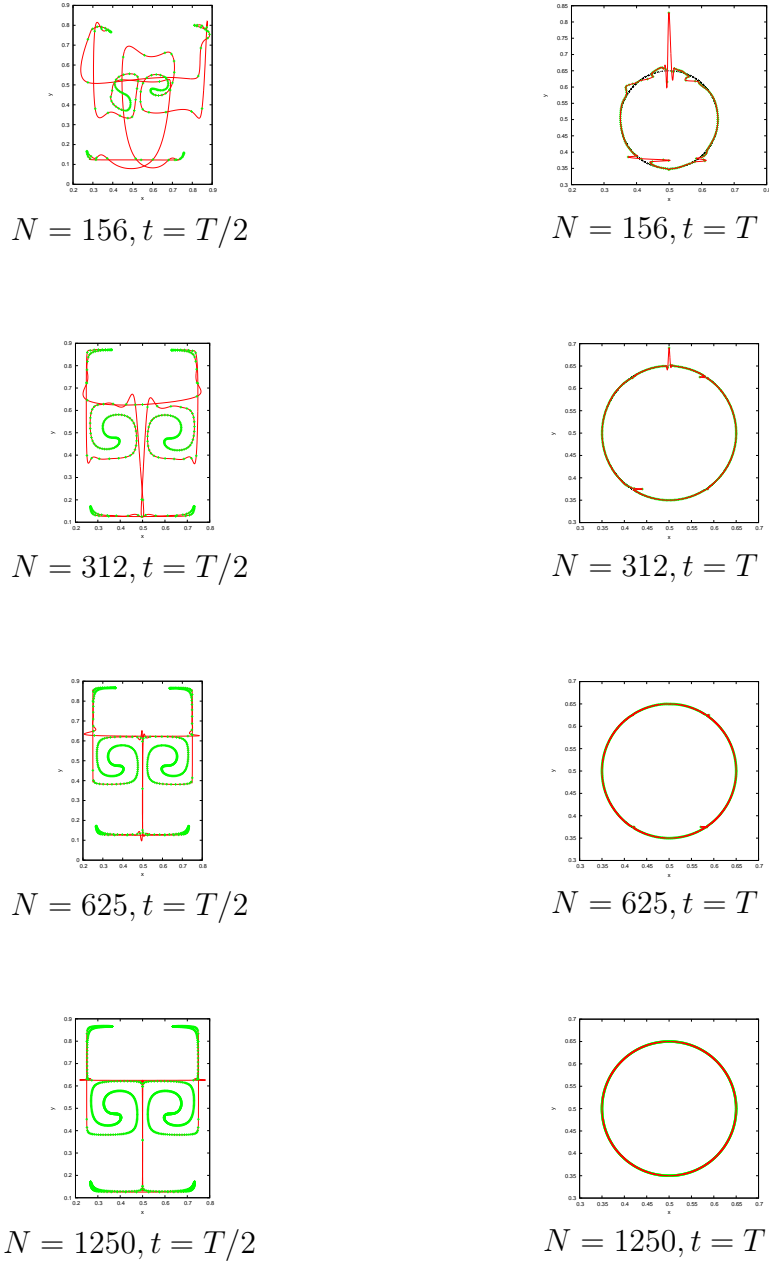


Figure 23: Result of the deformation field test for different resolutions N . The order of B-spline interpolation is $P = 3$. The graphs are shown at the maximal deformation, $t = T/2$ and after returning to the initial position $t = T$. The black dashed line is the exact solution for $t = T$.

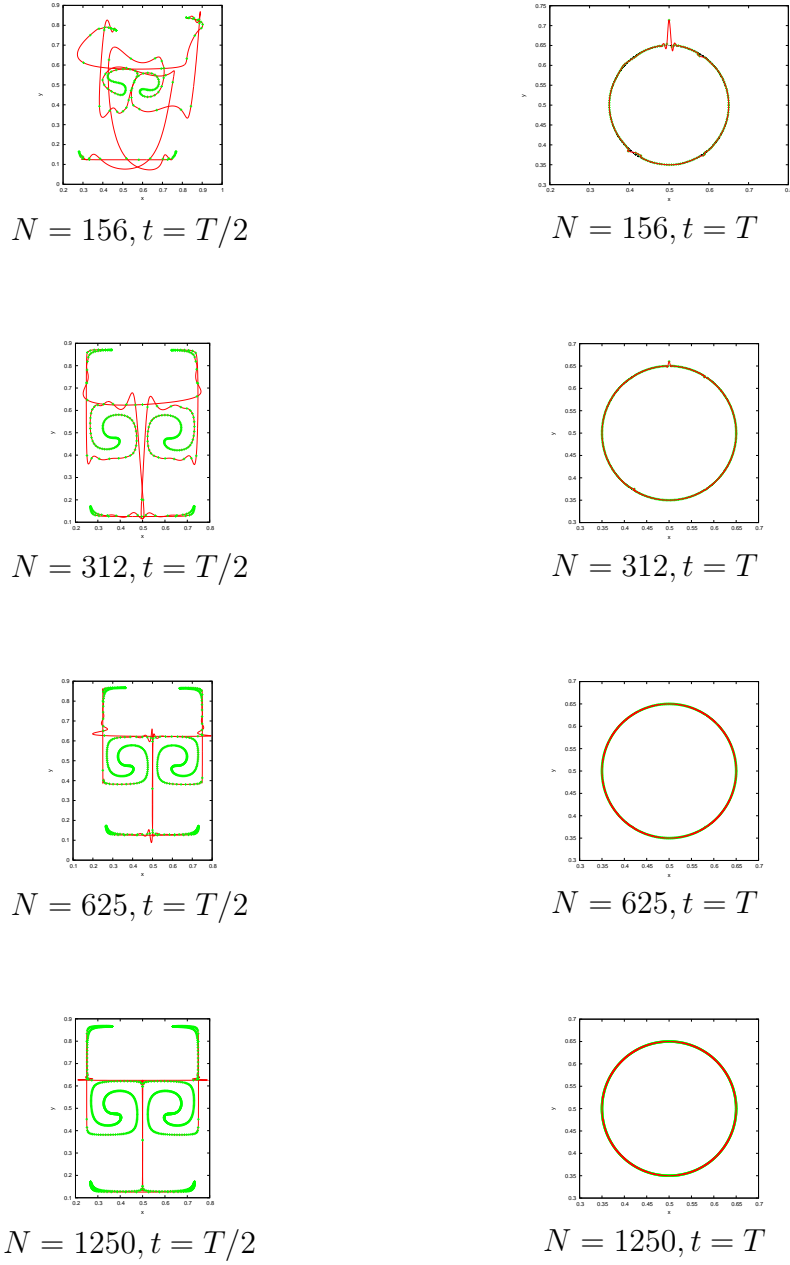


Figure 24: Result of the deformation field test for different resolutions N . The order of B-spline interpolation is $P = 5$. The graphs are shown at the maximal deformation, $t = T/2$ and after returning to the initial position $t = T$. The black dashed line is the exact solution for $t = T$.

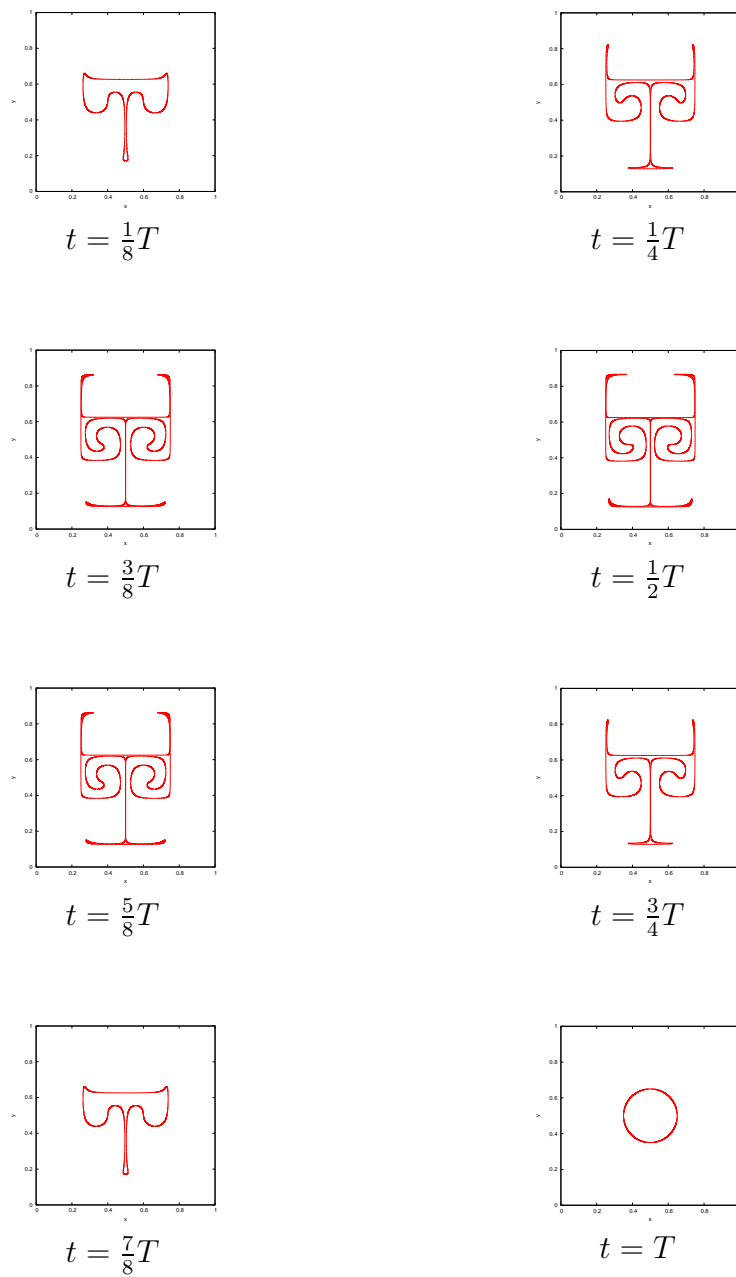


Figure 25: Results of the present method for the deformation field test at different points in time, here $N = 5000$ and $P = 5$.

P	N	Error	O
1	156	1.53946×10^{-3}	—
	312	6.86122×10^{-4}	1.17
	625	5.30438×10^{-5}	3.69
	1250	1.56053×10^{-5}	1.77
	2500	2.59629×10^{-6}	2.59
	5000	5.70028×10^{-7}	2.19
3	156	4.67185×10^{-3}	—
	312	4.27590×10^{-4}	3.45
	625	6.24600×10^{-5}	2.76
	1250	4.61800×10^{-6}	3.75
	2500	4.93238×10^{-7}	3.23
	5000	4.91313×10^{-8}	3.33
5	156	1.11787×10^{-3}	—
	312	1.14428×10^{-4}	3.29
	625	1.12848×10^{-5}	3.34
	1250	1.40122×10^{-6}	3.01
	2500	1.07634×10^{-7}	3.70
	5000	1.14465×10^{-8}	3.23

Table 5: Results for deformation field test for $P = 1, P = 3$ and $P = 5$.

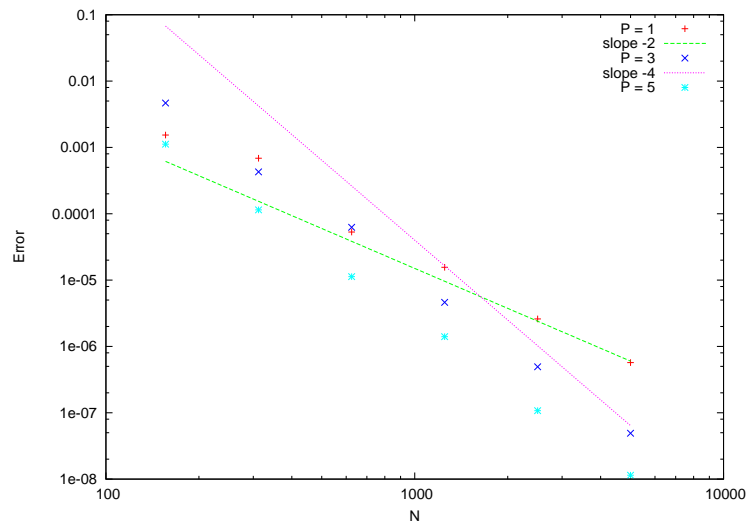


Figure 26: Error decrease for the deformation field test. The poorer convergence might be due to the appearance of spurious oscillations at regions of low resolution.

6. Conclusions

In the present discussion we derived an alternative formulation for the interface representation for the volume of fluid method. The interface is represented in a periodic fashion by two functions α and β , from which the position of the interface can be calculated. These two functions are approximated by periodic B-spline interpolation which allows a systematic extension to higher order accuracy with respect to the grid spacing. The advection scheme has been simplified and extended to higher order accuracy with respect to the time step. Numerical verification indicates that the present scheme has indeed the order of convergence predicted by the theory. This allows for very accurate simulations with a limited number of knots. However, if the sampling rate is too small, the present scheme can break down, providing a numerical solution far away from the exact one. In addition, for discontinuities in the first derivatives at a point on the interface, or at regions of the interface with poor resolution and high curvature, the present method can display a kind of Gibbs phenomenon. Taking a lower order B-spline interpolation $P = 1$ can in this case provide more appealing results. A remeshing or adaptive grid approach could increase the efficiency of the algorithm. In addition, such an approach might furnish a way to simulate topological changes such as coalescence or drop break up. The extension to three dimensions is also left for future research.

7. Acknowledgment

Thanks goes to Claudio Walker for interesting discussions. The author is grateful to Bernhard Müller for guidance and supervision.

References

- [1] J. Arvo, editor. *Graphics Gems II*. Morgan Kaufmann Academic Press, San Diego, 1991.
- [2] D. J. Benson. Volume of fluid interface reconstruction methods for multi-material problems. *Applied Mechanical Review*, 55(2):151–165, 2002.
- [3] T. Bjøntegaard and E. M. Rønquist. Accurate interface-tracking for arbitrary lagrangian-eulerian schemes. *Journal of Computational Physics*, 228:4379–4399, 2009.
- [4] T. Bjøntegaard, E. M. Rønquist, and Ø. Tråsdahl. High order interpolation of curves in the plane. *submitted*, 2009.
- [5] R. Courant and D. Hilbert. *Methoden der Mathematischen Physik I*. Springer-Verlag, Berlin, 1924.
- [6] S. J. Cummins, M. M. Francois, and D. B. Kothe. Estimating curvature from volume fractions. *Computers and Structures*, 83:425–434, 2005.
- [7] R. DeBar. Fundamentals of the kraken code. Technical Report UCIR-760, Lawrence Livermore Nat. Lab., 1974.
- [8] S. Diwarkar, S. K. Das, and T. Sundrarajan. A quadratic spline based interface (QUASI) reconstruction algorithm for tracking of two-phase flows. *Journal of Computational Physics*, 228:9107–9130, 2009.
- [9] P. A. Ferdowsi and M. Bussmann. Second-order accurate normals from height functions. *Journal of Computational Physics*, 227:9293–9302, 2008.

- [10] M. M. Francois, S. J. Cummins, E. D. Dendy, D. B. Kothe, J. M. Sicilian, and M. W. Williams. A balanced-force algorithm for continuous and sharp interfacial surface tension models within a volume tracking framework. *Journal of Computational Physics*, 213:141–173, 2006.
- [11] M. M. Francois and B. Swartz. Interface curvature via volume fractions, heights, and mean values on nonuniform rectangular grids. *Journal of Computational Physics*, 229:527–540, 2010.
- [12] J. López, J. Hernández, P. Gómez, and F. Faura. A volume of fluid method based on multidimensional advection and spline interface reconstruction. *Journal of Computational Physics*, 195:718–742, 2004.
- [13] G. Micula and S. Micula. *Handbook of Splines*. Kluwer Academic Publishers, 1999.
- [14] W. Noh and P. Woodward. Slic (simple line interface calculation). In *Proceedings of the 5th International Conference on Fluid Dynamics*, volume 59, pages 330–340, 1976.
- [15] G. M. Phillips. *Interpolation and Approximation by Polynomials*. Springer Verlag, New York, 2003.
- [16] W. H. Press, S. A. Teukolsky, W. T. Vetterling, and B. P. Flannery. *Numerical Recipes in C++*. Cambridge University Press, second edition, 2002.
- [17] G. Price, G. Reader, R. Rowe, and J. Bugg. A piecewise parabolic interface calculation for volume tracking. In *Proceedings of 6th Annual*

Conference of the Computational Fluid Dynamics Society of Canada,
Victoria, British Columbia, 1998. University of Victoria.

- [18] A. Quarteroni, R. Sacco, and F. Saleri. *Numerische Mathematik 2*. Springer Verlag, Berlin Heidelberg, 2002.
- [19] W. J. Rider and D. B. Kothe. Reconstructing volume tracking. *Journal of Computational Physics*, 141:112–152, 1998.
- [20] R. Scardovelli and S. Zaleski. Direct numerical simulation of free surface and interface flow. *Annual Review of Fluid Mechanics*, 31:567, 1999.
- [21] P. Smolarkiewicz. The multi-dimensional crowley advection scheme. *Month. Weather Rev.*, 110:1968–1983, 1982.
- [22] J. C. Verschaeve. Segment patching of the high order interface reconstruction for the volume of fluid method. In *Proceedings of the Fifth European Conference on Computational Fluid Dynamics*, 2010.
- [23] J. C. Verschaeve. High order interface reconstruction for the volume of fluid method. *Computers and Fluids*, in press.
- [24] J. C. Verschaeve. A third order accurate volume of fluid method. submitted.
- [25] T. Ye, W. Shyy, and J. N. Chung. A fixed-grid, sharp-interface method for bubble dynamics and phase change. *Journal of Computational Physics*, 174:781–815, 2001.
- [26] D. L. Youngs. Time dependent multi-material flow with large fluid distortion. *Numerical Methods for Fluid Dynamics*, pages 273–285, 1982.

- [27] S. Zalesak. Fully multi-dimensional flux corrected transport algorithms for fluid flow. *Journal of Computational Physics*, 31:335–362, 1979.
- [28] Q. Zhang and P. L.-F. Liu. A new interface tracking method: The polygonal area mapping method. *Journal of Computational Physics*, 227:4063–4088, 2008.

